Bulletin of the Seismological Society of America, Vol. 97, No. 1A, pp. S115–S127, January 2007, doi: 10.1785/0120050620

Slip of the 2004 Sumatra–Andaman Earthquake from Joint Inversion of Long-Period Global Seismic Waveforms and GPS Static Offsets

by Junkee Rhie, Douglas Dreger, Roland Bürgmann, and Barbara Romanowicz

Abstract The 26 December 2004 Great Sumatra–Andaman earthquake opened a new era for seismologists to understand the complex source process of a great earthquake. This is the first event with moment magnitude greater than 9 since the deployment of high-dynamic-range broadband seismic and Global Positioning System (GPS) sensors around the globe. This study presents an analysis of the ruptured fault-plane geometry and slip distribution using long-period teleseismic data and GPS-measured static surface displacements near the fault plane. We employ a rupture geometry with six along-strike segments with and without a steeper down-dip extension. The fault segments are further subdivided into a total of 201 $\sim 30 \times 30$ km fault patches. Sensitivity tests of fault-plane geometry and the variation in rupture velocity indicate that the dip and curvature of the fault plane are not well resolved from the given data set and the rupture velocity is constrained to be between 1.8 and 2.6 km/sec. Error estimations of the slip distribution using a random selection of seismic and GPS station subsets (50% of all stations) illustrate that slip is well resolved along the whole rupture and the mean slip uncertainty is less than 1.5 m (about 11%). Although it is possible that near-field GPS data include contributions from additional postseismic transient deformation, our preferred model suggests that the Sumatra–Andaman earthquake had a magnitude of M_w 9.20 + 0.05/−0.06.

Online material: Comparison of slip models, GPS modeling, waveform fit, fault geometry, and inversion parameters.

Introduction

The great M_w 9.1–9.3 Sumatra–Andaman earthquake occurred on 26 December 2004 in the subduction zone west of the island of Sumatra in Indonesia rupturing northward for about 1300 km along the Nicobar–Andaman island chain (Lay *et al.*, 2005). It is the first great event with sufficient data to allow for a detailed analysis of its complex source-rupture process. For the first time, global very broadband seismic and geodetic measurements are available. Several slip and rupture propagation models have been estimated from short-period *P* waveforms (Ishii *et al.*, 2005; Krüger and Ohrnberger, 2005; Lomax, 2005; Ni *et al.*, 2005), hydroacoustic *T*-phase data (de Groot-Hedlin, 2005; Tolstoy and Bohnenstiehl, 2005), long-period normal modes (Park *et al.*, 2005; Stein and Okal, 2005), long-period waveforms (Tsai, *et al.*, 2005), broadband seismic waveforms (Ammon *et al.*, 2005; Lay *et al.*, 2005), and geodetic data (Banerjee *et al.*, 2005; Vigny *et al.*, 2005; Subarya *et al.*, 2006). In this article we jointly invert the long-period teleseismic waveform data and horizontal static-surface offsets from campaign-mode and continuous GPS observations in the near-field region of the event for the coseismic slip distribution, and perform a sensitivity and error analysis of fault geometry, slip distribution, and kinematic rupture parameters.

Data and Inversion Method

We considered all three components of displacement recorded at 10 Incorporated Research Institutions for Seismology (IRIS) and GEOSCOPE seismic stations (Figure 1a). The epicentral distances, measured from the U.S. Geological Survey (USGS) epicenter (95.96° E, 3.30° N) to the 10 stations range from 43.6° (AAK) to 65.2° (TAU). The 10 stations were selected by considering their signal-to-noise and azimuthal coverage qualities. From each station three-component waveforms for a 4000-sec time window from the origin time were used. The data and theoretical Green's functions were bandpass filtered between 100 and 500 sec. We computed theoretical Green's functions at 0.2° intervals in distance and 5-km intervals in depth by using the normal-mode summation method in spherical geometry with model PREM (Dziewonski and Anderson, 1981). Because PREM is

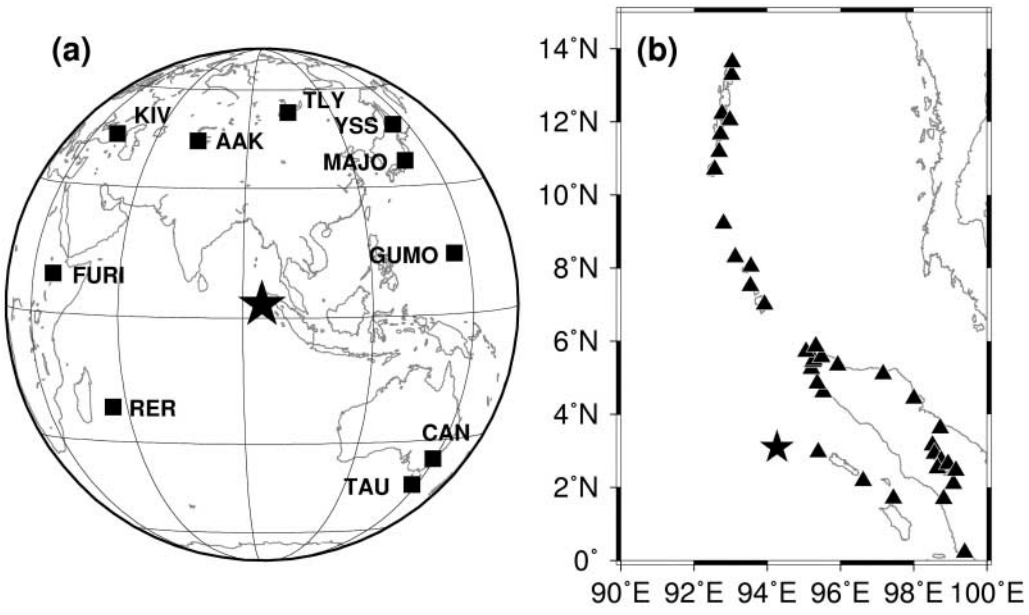

Figure 1. Location of seismic (a) and GPS (b) stations included in inversion. Epicenter is indicated with star.

a very good average 1D model for long-period seismic waveforms, we didn't take into account any 3D wave-propagation effects on our Green's function computation.

The GPS data used for the inversion represent a 38-station near-field subset of the 142 coseismic surface displacements measured by continuous and campaign-mode GPS stations reported by Banerjee *et al.* (2007) (Fig. 1b). We focus on the near-field horizontal geodetic data, including campaign and continuous GPS measurements on the Sumatra, Nicobar, and Andaman Islands from within 300 km of the trench and between 0° N and 14° N. In this data set the offset estimates for near-field campaign-mode GPS sites were adjusted using an after-slip model to account for several weeks of postseismic deformation prior to reoccupation of the GPS stations (Banerjee *et al.*, 2007; their tables S-3 and S-4). The distribution of vertical GPS offsets can provide valuable constraints on the dip and extent of the fault plane. However, corrections for postseismic components of the vertical offsets at near-field sites are not available. Therefore, vertical offsets are just used to crosscheck the reliability of final models (Ⓔ see Figures S1 and S2 in the electronic edition of BSSA). GPS Green's functions for flat-layered elastic structures based on PREM are computed using FORTRAN programs EDGRN/EDCMP (Wang *et al.*, 2003). Although the length of our fault model is very long and Earth sphericity can be important, we found that static offsets are insensitive to slip further than 400 km from a GPS station (Ⓔ see Figure S3 in the electronic edition of BSSA). Therefore it is justifiable to ignore sphericity for the near-field GPS stations (within 400 km) of the fault. Modeled displacements of stations at much greater distances with centimeter-level offsets would be greatly underpredicted unless Earth sphericity is taken into account (Banerjee *et al.*, 2005, their figure S3).

To invert data for the slip distribution, we use a least-squares inversion method, which has been widely applied for source studies using locally or regionally recorded earthquakes with or without additional geodetic constraints (e.g., Hartzell and Heaton, 1983; Dreger and Kaverina, 2000; Kaverina *et al.*, 2002). Here we use normal-mode-computed Green's functions, as described subsequently, to invert complete waveforms at teleseismic distances.

Seismic waveforms and GPS static offsets can be represented by a space–time and space convolution of slip and Green's functions, respectively. For fixed fault planes and predefined rupture initiation time at each subfault based on rupture velocity, origin time, and relative location with respect to hypocenter, observed seismic waveforms and GPS offsets can be represented by

$$U(x,t) = \sum_{n=1}^{N} \mu_n A_n u_n \cdot G_S(x, x_n, t + \delta t_n),$$

$$V(x) = \sum_{n=1}^{N} u_n \cdot G_G(x, x_n).$$

$U(x,t)$ and $V(x)$ are the observed seismic waveform and GPS offset at a station location of x. G_S and G_G are seismic and GPS Green's functions, δt_n is the time delay due to rupture propagation, and x_n is a subfault location. A_n, μ_n, and u_n are subfault area, rigidity, and slip for the nth subfault from a total of N subfaults, respectively. These equations are discrete forms of the general representation theorem. Here all other parameters except u_n are given. Therefore, a simple

matrix relation between observed data (waveforms and GPS offsets) and model parameter u_n can be constructed (Kaverina *et al.*, 2002). Because we are inverting long-period data, and the rise time of each subfault is very short (e.g., Sommerville *et al.*, 1999) compared with the passband (100–500 sec) employed, the detailed variation in slip rise time of each subfault is not recoverable with the long-period data and ignored. The trigger time of each subfault is defined by the passage of the circular rupture front with constant rupture velocity over one fault segment. There is a broad range (1.8–2.6 km/sec) of rupture velocities that fits the seismic waveform data we used. We choose the value of 2.5 km/sec because it is consistent with the *T* phase (Tolstoy and Bohnenstiehl, 2005) and short-period *P*-wave observations (Krüger and Ohrnberger, 2005; Ni *et al.*, 2005). For multiple-segment fault models, initial points of the rupture front on each segment account for the transit times across previous segments with respect to the origin time. A Laplacian-smoothing operator and slip-positivity constraint are applied in all of the inversions. For the joint inversion, a weighting factor is applied to the geodetic data set and GPS Green's functions to find an optimal slip model sufficiently explaining both data sets.

Distributed Slip Models Obtained from Seismic and Geodetic Data

We test two fault geometries. Geometry model A is obtained from the previous study of Banerjee *et al.* (2005) and model B is slightly modified from model A in that the deeper, steeper segments of the fault have been removed (small panels in Fig. 2a and b). Model A consists of 12 fault segments with 6 segments along the trench-parallel direction and 2 down-dip segments. This fault geometry takes increasing dip angles with depth into consideration. Geometry model B consists of 6 segments. Each segment in this model has the same upper-edge location, strike, dip, and length parameters as the upper segments of model A, but the down-dip width is increased by 20 to 33% to maintain the total width of model A (Ⓔ Table S1 in the electronic edition of BSSA). Thus, the dip angles of the segments are constant with depth for model B. The dip angles of the segments are 11, 15, 18, 18, 18, and 18° from south to north and 35° for all deeper segments of model A. Each segment of the fault model is further divided into subfaults with length and width of about 30 km for the inversion. The total number of subfaults is 201. This level of subfault discretization corresponds to the lower cutoff period of the seismic-waveform data with respect to seismic-wave velocity and the range of rupture velocity. It also produces a smooth kinematic rupture model in the passband employed. The rake is allowed to vary within the range of 50° to 140° with respect to the strike.

We name the slip models depending on the choice of fault geometry and inclusion of the seismic and/or GPS data. Slip model AS refers to the model inverted from seismic data only over geometry A, the slip model on geometry A from only GPS data is model AG, and model BJ indicates a slip model for geometry model B derived from the joint inversion of seismic and GPS data.

We find that the slip distributions obtained with the two different fault geometries, using only long-period seismic waveform data (slip models AS and BS) are very similar (Fig. 2) because long-period waveforms are not sensitive to the small variation in dip angles with depth. Although these models were obtained by inverting only the primary wave field, including R_1 and G_1 (initial 4000 sec of record), they were also found to forward model well the later-arriving waveforms over a long time window of about 4 hours (15,000 sec). Even though there are about four times more data points in 4-hour records than there are in 4000-sec records, the variance reduction is only lower by 6%. In Figure 2, both slip models AS and BS show large slip patches at about 4° N and a high-slip region with slip larger than 10 m extends only up to 10° N. There is no indication of substantial slip on the northern fault segments. Slip near the hypocenter is small compared with the largest slip further to the north within the southernmost fault segment. The rake changes from south to north. On the southern segment (2° N–5° N), the slip direction is nearly pure dip slip. However, it becomes more oblique (reverse plus right-lateral) on the next two northern segments (5° N–10° N). The moment magnitudes (Hank and Kanamori, 1979) of slip models AS and BS are 9.14 (5.783×10^{29} dyne cm) and 9.12 (5.287×10^{29} dyne cm), respectively.

The seismic-variance reductions for the given slip models show that all three-component variance reductions vary significantly with azimuth (different stations). The variance reductions may be affected by two main factors, namely, directivity and the radiation pattern. The variance reductions for all three components have significant troughs near the direction opposite to the rupture propagation (e.g., azimuth ~140°, CAN and TAU). The source time function at these stations is longer and more complex than the one recorded at a station in the rupture direction, due to directivity (Fig. 3a and c). The comparison between the trend of tangential variance reduction and the *SH*-radiation pattern based on the single Harvard CMT solution shows a correlation with minima in the CMT *SH* radiation and the level of fit to the waveforms from the finite-source rupture models (Fig. 2c and d). This indicates that the observed waveforms at stations located near radiation nodes contain some 3D wave-propagation effects due to heterogeneity, focusing, and defocusing. The comparison of synthetic and observed seismic waveforms shows that synthetic waveforms underestimate observed waveforms near *SH* nodes (e.g., YSS, MAJO, KIV, and AAK) for the tangential component, whereas the synthetics for radial and vertical components fit the corresponding observations well, except in the direction opposite to the rupture (Fig. 3 and Ⓔ Figures S4 and S5 in the electronic edition of BSSA).

To better constrain the slip distribution we added geodetic static offset data. In combining the two data sets it is

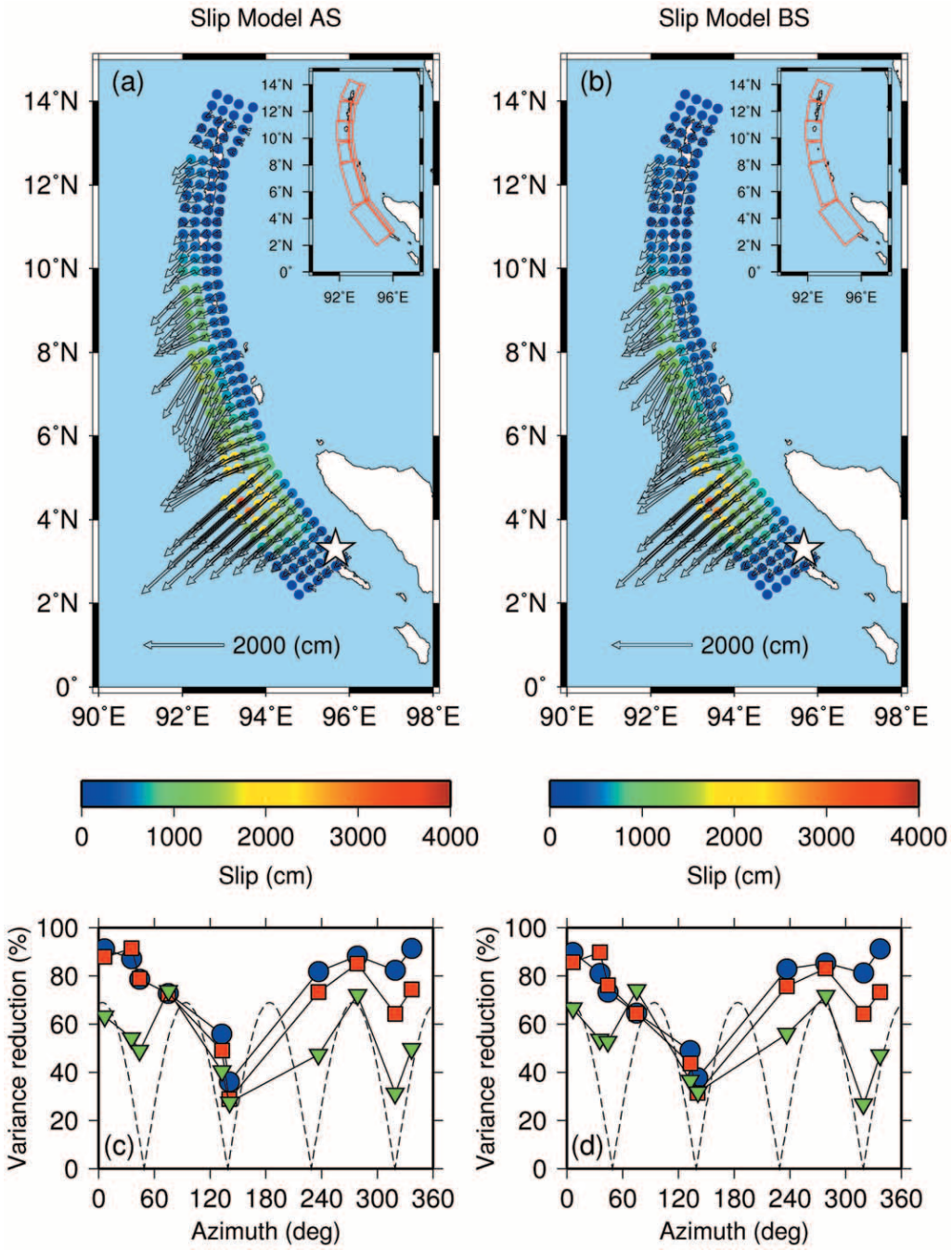

Figure 2. (a) Slip-distribution model from seismic-waveform inversion only (model AS) over fault-geometry model A. The fault geometry A (small panel) is obtained from previous work (Banerjee *et al.*, 2005). A white star indicates the epicenter. Color represents total slip and the arrows show the slip vector. (b) Same as (a) for fault-geometry model B. The geometry of model B (small panel) is modified from model A and does not allow for changes in dip with depth. (c) Variance reduction at 10 seismic stations ordered by azimuth for slip model A. Vertical, radial and tangential variance reductions are plotted with circles, squares, and triangles, respectively. The dotted line shows the *SH*-radiation pattern for the Harvard CMT solution. Total variance reduction is 70.43%. (d) Same as (c) for slip model B. Total variance reduction is 71.65%.

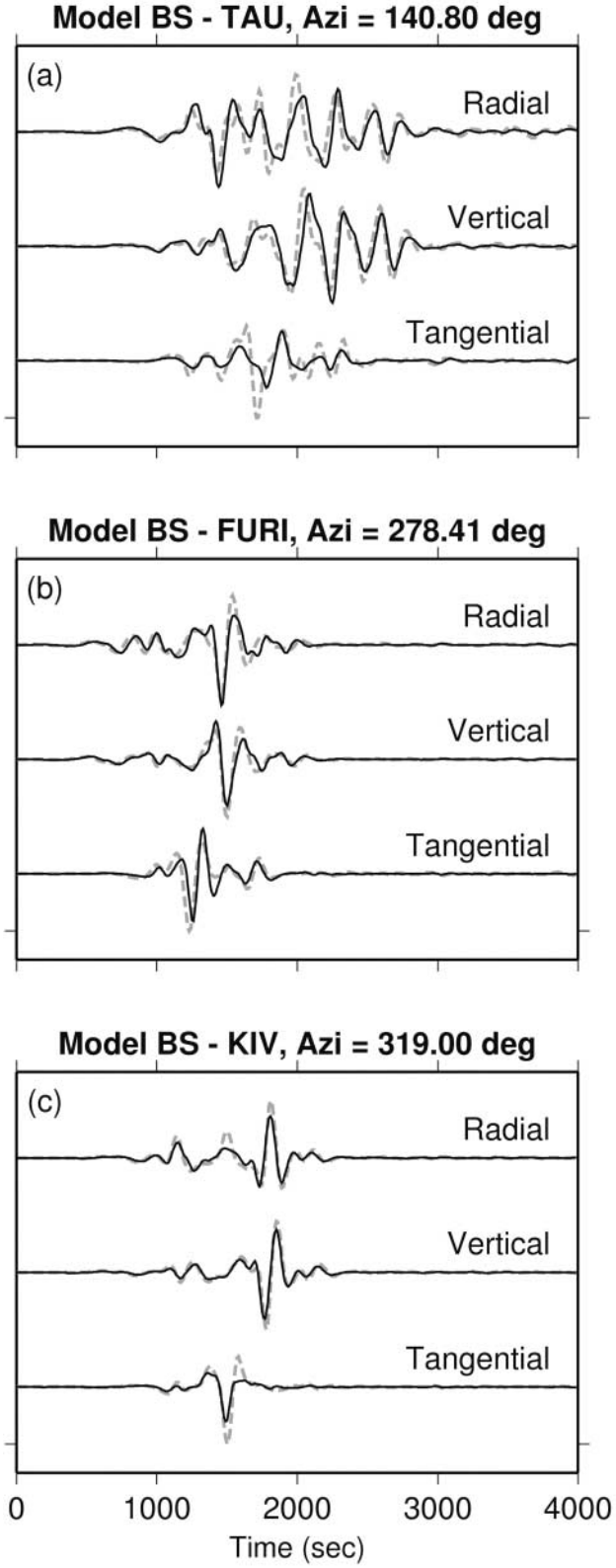

Figure 3. Comparison of three components of synthetic (solid) and observed (dotted) seismic waveforms for three selected stations located in a direction nearly opposite to that of rupture propagation (TAU), *SH* lobe (FURI), and node (KIV). Time starts from the origin time of the event (2004.361, 00:58:53 [UTC] from USGS). For a comparison between observed and synthetic waveforms for all of the stations (Ⓔ see Figures S4 and S5 in the electronic edition of BSSA).

necessary to apply a relative weight (GPS weight) to account for the different amount of information in the two data sets. We performed a sensitivity analysis of the GPS weight regarding the respective levels of fit to each data set. An optimal weight was found that resulted in good, near-maximum levels of fit to the two independent data sets (Fig. 4a). For the joint inversion of seismic waveforms and GPS, two variance-reduction curves clearly show trade-offs as a function of GPS weight; as the GPS weight increases so does the fit to the GPS data, whereas the fit to the seismic-waveform data decreases by a smaller amount. The seismic moment increases as the weight increases (Fig. 4b), indicating that the GPS data require greater seismic moment. From the trade-off curves (Fig. 4a), we choose a GPS weight of 0.8, which results in large variance reduction for both the seismic and GPS data sets, for both fault-model geometries. We refer to these joint-inversion models as AJ and BJ.

The variance reductions for the two GPS-only models AG and BG are both 99.9%. Seismic moments for slip models AJ, BJ, AG, and BG are 7.685×10^{29}, 7.152×10^{29}, 8.374×10^{29}, and 8.461×10^{29} dyne cm, respectively. The M_w of the joint inversions is 9.21 and for the GPS-only inversions it is only slightly larger (9.25). These values are larger by about 50% than the corresponding moments from models using only seismic data, but all the inversions indicate that the M_w lies in a range from 9.12 to 9.25.

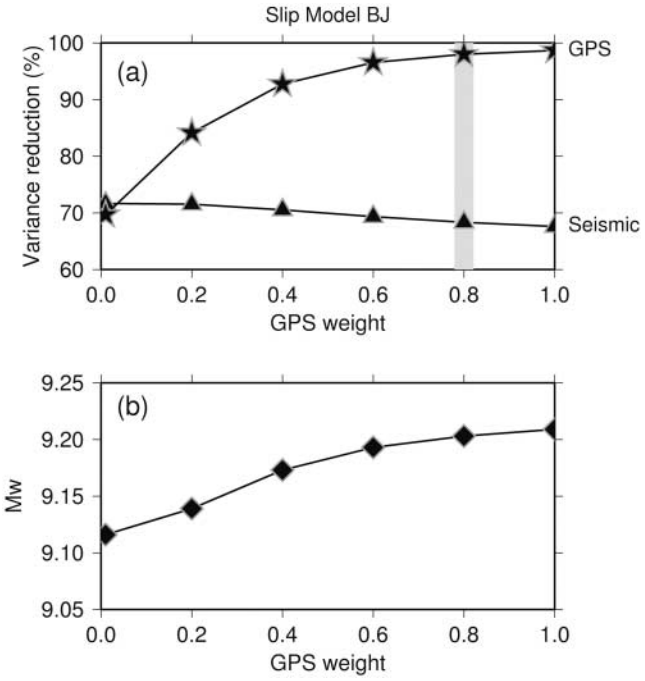

Figure 4. GPS weighting. (a) Variance reduction of seismic waveforms (triangles) and GPS (stars) is plotted against the GPS weight for model BJ. The preferred GPS-weighting factor is highlighted with the gray bar. (b) Variation in moment magnitude with GPS weight for model BJ. The variation in variance reduction and seismic moment with weighting for model AJ are very similar.

To evaluate the differences among slip models from the different data sets we plot changes in moment density with latitude (Fig. 5a and Ⓔ Figure S6a in the electronic edition of BSSA). Moment density is defined as released moment per kilometer along strike from south to north. The trends of moment density for models AJ and BJ are similar to the seismic-slip models but the moment density of the joint-inversion slip models are substantially higher than the seismic models in the northern part of the rupture, especially with respect to the maximum-moment release (about 4° N). The slip models from GPS-only inversions show significant moment release near the epicenter (about 3° N). The joint and GPS slip models differ in that the GPS models show larger moment released on the southern (about 2° N) and central (5–10° N) part of the fault but less moment release near the maximum found in the joint inversions (4° N) (Fig. 5a and Ⓔ Figure S6a in the electronic edition of BSSA). The total seismic-variance reductions are 68.39 (slip model AJ) and 68.36% (slip model BJ), which are lower by 1.0 and 3.3% than those obtained in the seismic-waveform-only inversions (Fig. 5b and Ⓔ Figure S6b in the electronic edition of BSSA). However the GPS-variance reductions for the two models are 96.39 and 98.00%, which are increased by 23.86 and 28.37% from the forward-modeled GPS using the seismic-only slip models (AS and BS). The variations in seismic-variance reductions for the three components show that the variance reductions are more or less consistent with those for slip models AS and BS, but the variance reductions of all three components have more significant minima near 140 deg (opposite direction of the rupture propagation) and near one of the *SH* nodes at 320 deg. The modeled GPS offsets for slip models AJ and BJ underestimate the GPS offsets over the fault plane. (Fig. 5c,d and Ⓔ Figure S6c,d in the electronic edition of BSSA).

Sensitivity Tests for Fault Geometry and Rupture Velocity

To confirm that our choice of fault geometry is not generating any artificial moment distribution due to inappropriate distribution of subfaults or extent of the segments, we tested several fault-geometry models, which are perturbed from model B. These tests (Ⓔ see Figure S7 in the electronic edition of BSSA) show that the effect of extending the fault planes is not significant compared with laterally shifting the whole-fault planes. A shift of the model fault planes by 0.2° (~22 km) to the east and west reduces and increases the seismic moment, respectively. It indicates that the relative distance from shallow subfaults to the GPS stations that have large static offsets mainly control the seismic moment of the models (Ⓔ see Figure S7 in the electronic edition of BSSA). The extension of the length of the southern-most segment and down-dip extension do not change the fit to the seismic and GPS data sets and the changes in seismic and GPS-variance reductions are less than 1 and 3%, respectively. The shifting of the whole-fault plane does not improve the fit to GPS static-offset data, but seismic data prefer the model shifted to the south. The seismic-variance reduction is increased by 3% compared with that for model B.

To constrain key model parameters, we also consider sensitivity tests for dip angle and rupture velocity. Both parameters are important in the estimation of moment magnitude and final slip distribution. First, we test a series of dip angles that were jointly varied for all segments in geometry model B. Repeated inversions with changes in dip over a range of $\pm 8°$ from the starting model show that the variance reduction is slowly decreasing as dip angle is increasing (Fig. 6a). However, we find a systematic increase in moment magnitude with decreasing dip as had been previously documented (Fig. 6b) (Banerjee *et al.*, 2005). The dip angles of the fault planes are very important to determine the seismic moment of this earthquake. Gentle dip angles can lead to quite a large seismic moment (Tsai *et al.*, 2005). Although the sensitivity test for dip angle indicates that a shallower rupture plane leads to an improved fit of the teleseismic waveforms when it is jointly constrained with near-horizontal static offsets, we still prefer the fault-geometry model with unperturbed dip angles because this fault geometry is compatible with the distribution of aftershocks (Bilham *et al.*, 2005; Lay *et al.*, 2005; Engdahl *et al.*, 2007). We also tested many models in which dip angles were independently varied in geometry model B, but our data set is not sensitive enough to resolve the detailed variation in dip angles over the fault segments.

Finally, we test seismic- and GPS-variance reduction and seismic moment as a function of rupture velocity (Fig. 6c–f). We consider joint inversions of the three-component seismic waveforms and the GPS data and seismic-only inversions for geometry models A and B. For both fault geometries the best fit is over the range from 1.8 to 2.8 km/sec, showing that the data set we used is not very sensitive to the rupture velocity, though it is clearly subshear. The seismic-only results show a trend that is similar to the ones obtained for the joint inversions. Note, however, that the forward-modeled GPS offsets using the seismic-only slip model results in a sharp peak in variance reduction at 2.5 km/sec (Fig. 6e). This indicates that the slip distribution obtained from seismic data using a 2.5 km/sec rupture velocity can explain the near-field static offsets relatively well. Although our sensitivity test did not give us an optimal rupture velocity, we believe that a 2.5 km/sec rupture velocity is reasonable based on forward GPS computations and also independent previous estimations based on different data sets (Ammon *et al.*, 2005; Krüger and Ohrnberger, 2005; Ni *et al.*, 2005; Tolstoy and Bohnenstiehl, 2005). Because the seismic and geodetic data we consider do not provide good constraints on either the dip or the propagation velocity of the rupture, it is important to incorporate independent determinations of these parameters from other studies (e.g., Bilham *et al.*, 2005; Ishii *et al.*, 2005; Tolstoy *et al.*, 2005; Engdahl *et al.*, 2007).

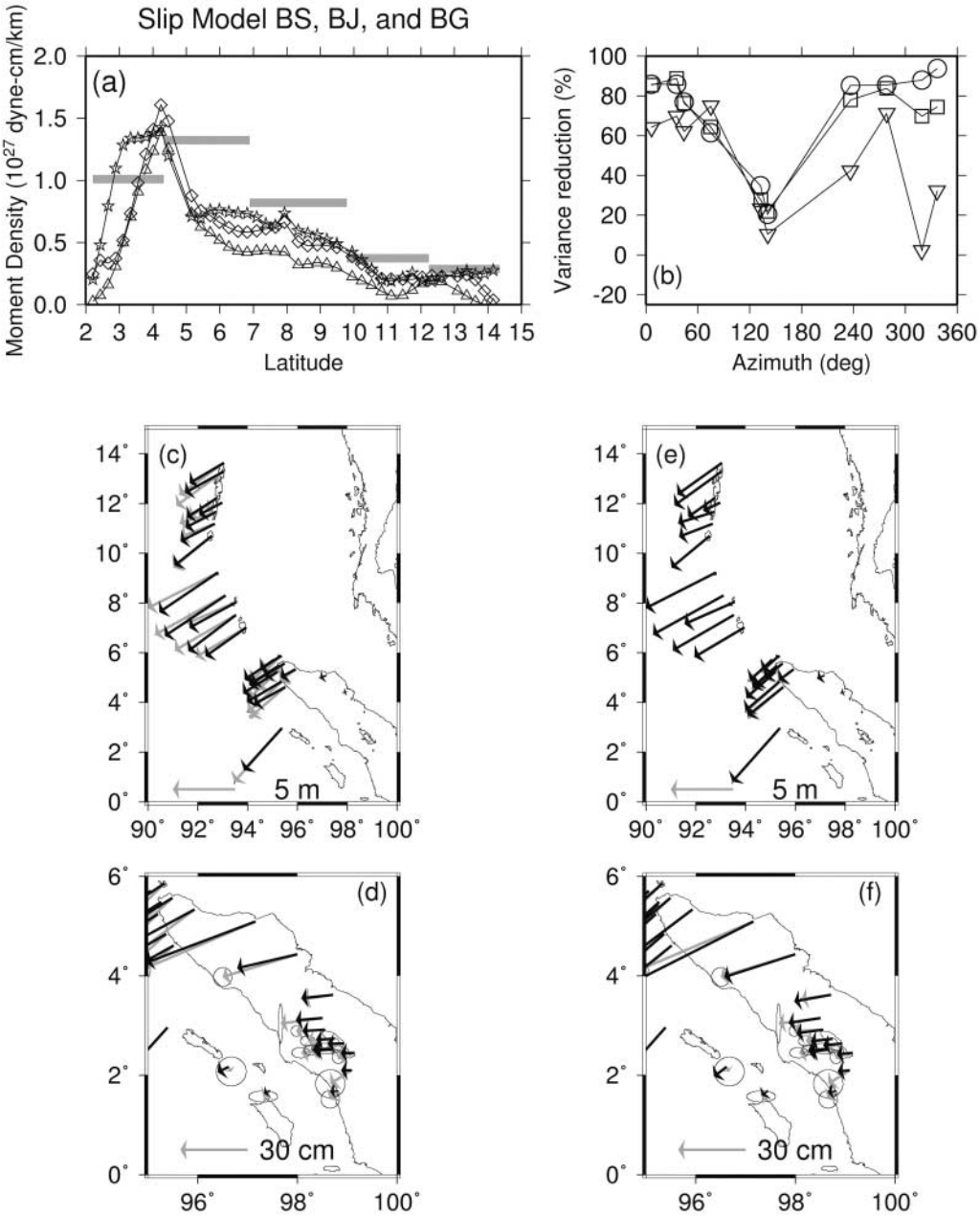

Figure 5. (a) Moment density with latitude for model BS (black line with triangles), BJ (diamonds), and BG (stars). Here, symbols indicate latitude of the upper most subfaults. For reference, moment density from the multiple CMT solution of Tsai *et al.* (2005) is plotted with gray bars. Because the multiple CMT sources have a gentler dip than our fault-plane models do, the moment density for the multiple CMT solution is larger than that obtained from only seismic waveforms in this study (see Fig. 6b). (b) The fit (variance reduction) to vertical (circles), radial (squares), and tangential (inverse triangles) waveforms for all stations is plotted as a function of azimuth. The total seismic-variance reduction is 68.36%. (c) Comparison of observed (gray) and best fitting GPS vectors (black) for model BJ. The total GPS variance reduction is 98.00% (d), same as (c) for northern Sumatra Island. (e) Same as (c) for slip model BG. (f) Same as (d) for slip model BG. The total GPS variance reduction is 99.98%. For model A (Ⓔ see Figure S6 in the electronic edition of BSSA).

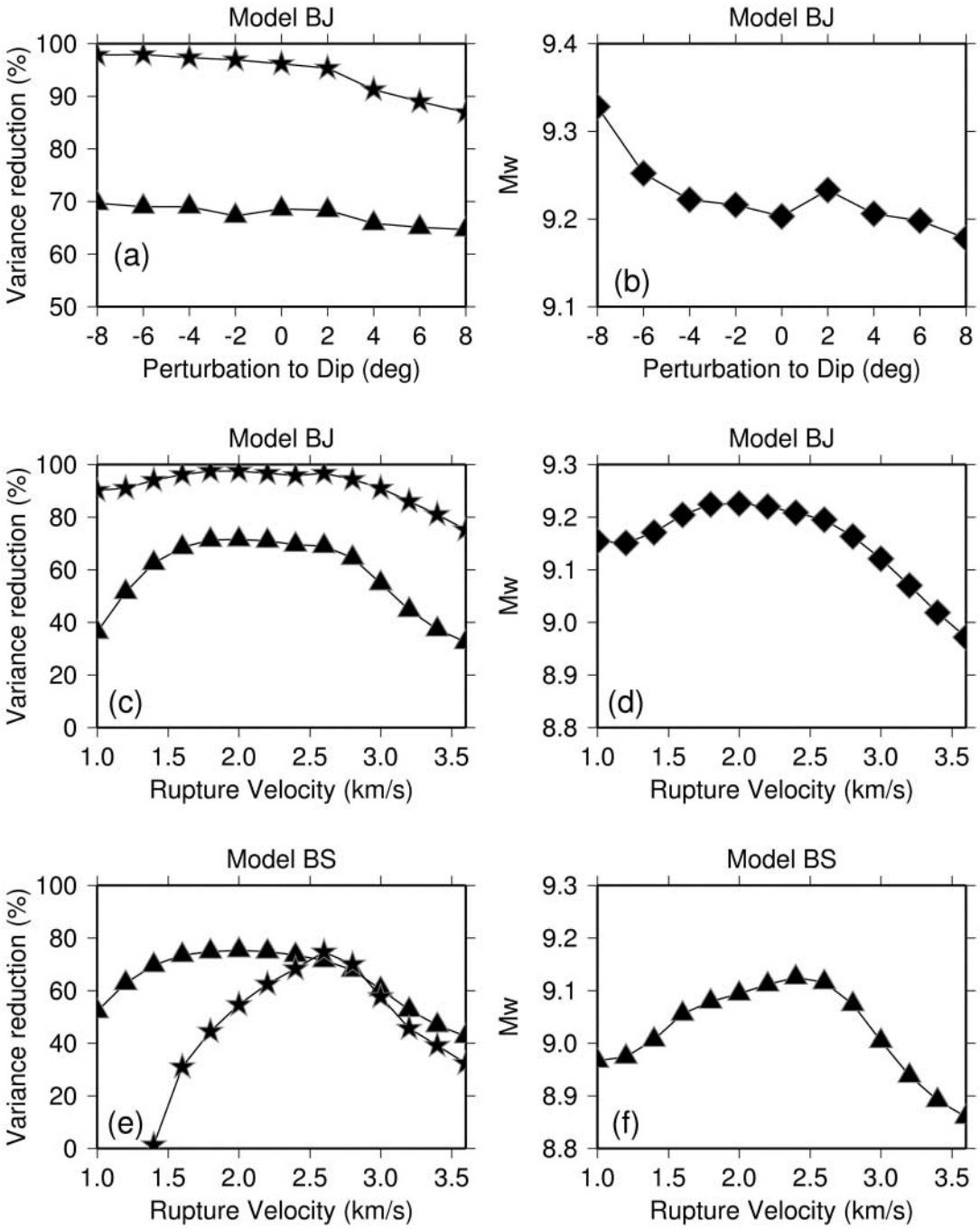

Figure 6. (a) Data fit (GPS, stars; seismic, triangles) is plotted against the perturbation in dip angle from the fault-geometry model B. Negative dip perturbation indicates shallower dip. (b) M_W is compared with perturbation to dip. (c) Fit versus rupture velocity for fault-geometry model B (symbols have same meaning as in a). (d) Variation in moment magnitude with rupture velocity. (e) Same as (c) for seismic-data-only inversion. Here the GPS variance reduction is obtained by forward computation. (f) Same as (d) for seismic-only inversion.

Error Analysis using Random Station Selection

A proper estimate of model error is as important as getting a very detailed slip distribution. However, it is not easy to conduct a complete error analysis for slip-distribution models because many factors contribute, such as the assumed velocity model or the station geometry. Here we investigate the variability in recovered slip due to the choice of stations used in the inversion. In this random station-selection method we randomly select 50% of seismic and

GPS stations and invert them for slip distribution and we repeat this process ten times. (Each inversion takes about 12 hours to compute, and thus we did not conduct more comprehensive statistical subsampling tests.) By doing this, we obtained 10 slip-distribution models from which the mean and standard deviation of the slip was computed (Fig. 7 and Ⓔ see Figure S8 in the electronic edition of BSSA). The mean slip distribution is very similar to the preferred joint inversion. The estimates of seismic moment (M_0) and 1 standard deviation errors are $7.425 \pm 0.405 \times 10^{29}$ (M_w 9.21 $-0.02/+0.02$) and $6.963 \pm 0.433 \times 10^{29}$ (M_w 9.19 $-0.02/+0.02$) for slip models AJ and BJ, respectively. The uncertainty of slip at each subfault is computed by taking 1 standard deviation. The maximum and mean slip errors for model AJ(BJ) are 394(440) cm and 115(123) cm. This indicates that our slip distribution is stable with respect to the choice of the seismic and GPS stations. For both slip models AJ and BJ, maximum uncertainty of slip occurs near the surface of the southern segments near 4° N.

Discussion and Conclusions

We invert long-period global seismic waveforms and static horizontal GPS offsets for the slip distribution of the 2004 Sumatra–Andaman event. The results show that the mean total seismic moment from models AS, BS, AJ, BJ, AG, and BG is $7.124 \pm 1.330 \times 10^{29}$ (M_w 9.20 $+0.05/-0.06$). The estimate of M_w 9.20 is consistent with that obtained by Banerjee *et al.* (2005, 2007) and Vigny *et al.* (2005) using only GPS data. The mean M_w from the seismic-only, joint, and GPS-only inversions are 9.13, 9.21, and 9.25. The discrepancy between models using seismic-only and joint data sets indicates that some slip may not be detected in the seismic waveforms in the period range between 100 and 500 sec, but uncertainty due to the assumed velocity structure and possibly unaccounted for postseismic deformation could also account for the difference. To explain this moment-magnitude difference, we need approximately 2–3 m of additional slip on nearly the whole fault surface, which corresponds to an increase of about 32% of the average slip over the seismic-only models. The near-field coseismic GPS offset estimates of Banerjee *et al.* (2007) include a correction for afterslip based on an inversion of available continuous GPS displacements from between the time of the earthquake and the GPS campaign observations. It is possible, however, that some additional afterslip affecting some of the near-field sites is not captured in this model. Vigny *et al.* (2005) show from epoch-by-epoch analysis of the first few hours of GPS time series, that the event did not involve significant continued slow slip, which had been suggested by Stein and Okal (2005) to explain systematic increases of moment estimates with the period of the data considered. As we mentioned in the section on sensitivity tests for fault geometry and rupture velocity, the dip angle of the fault is a very important parameter that controls the seismic moment of the earthquake and it is possible to estimate a quite large moment magnitude when a gentler fault plane is assumed (e.g., Tsai *et al.*, 2005).

We compare forward-modeled static offsets at far-field sites from the slip models we derived in Figure 8. Because our GPS subset is restricted to near-field stations, we test if our slip model can explain relatively far-field GPS offsets on the Malaysian Peninsula, which were used in previous geodetic slip inversions (Subarya *et al.*, 2005; Vigny *et al.*, 2005; Banerjee *et al.*, 2007). We do not consider station offsets at >1000-km distance, as their motions are strongly affected by Earth's sphericity, which we do not incorporate in our static-offset model. Subarya *et al.* (2005) examined both layered and homogeneous half-space models, whereas Vigny *et al.* (2005) relied on uniform elastic half-space calculations. The forward GPS prediction for models AS (Ⓔ see Figure S9 in the electronic edition of BSSA) and BS (Fig. 8), which significantly underestimate the near-field GPS observations (Fig. 8a), slightly underestimate the far-field offsets, whereas models AJ, BJ, AG, and BG, which are optimized to fit the near-field GPS offsets (Fig. 5c and e, and Ⓔ Figures S6c and S6e in the electronic edition of BSSA), slightly overestimate the GPS observations over the Malaysian Peninsula (Fig. 8c and d). However, as the comparison shows, our slip model from the joint inversion of seismic waveforms and near-field GPS offsets can explain the far-field static offsets quite well. The good fit to both the near-field campaign data corrected for postseismic motions and to the 1-day offsets of permanent GPS stations in the far field suggests that any unaccounted for postseismic excess motions are small.

Banerjee *et al.* (2005, 2007) find that slip on steeper-dipping segments at depth below portions of the rupture improve the fit to the GPS deformation data, especially in the vertical component. We tested the two fault-geometry models with varying and constant dip angles. The nearly identical slip models for fault-geometry models A and B (Fig. 2 and Figures S1 and S2 in the electronic edition of BSSA) indicate that the frequency range of our seismic data set is too low to independently resolve the increasing dip of the plate interface with depth and our near-field horizontal component GPS offset data are also not sensitive to the variation in dip angle with depth.

Our joint slip distribution (Fig. 9) is similar to slip models obtained from other studies in that the location of largest slip patch and the extent of the large slip region (e.g., Ammon *et al.*, 2005; Song *et al.*, 2005). The largest slip patch, just west of the northern tip of Sumatra, is consistent with one of the tsunami source regions found by Fine *et al.* (2005), and the northward extent of significant slip in our joint-inversion models is consistent with the tsunamigenic regions proposed by Lay *et al.* (2005).

Our investigation of the sensitivity of the obtained slip models to geometry, rupture velocity, as well as seismic-station distribution indicates that the joint-inversion models for the two possible fault geometries are well constrained, where maximum deviations are on average less than 1.5 m over all fault segments. The maximum slip is near 4° N and

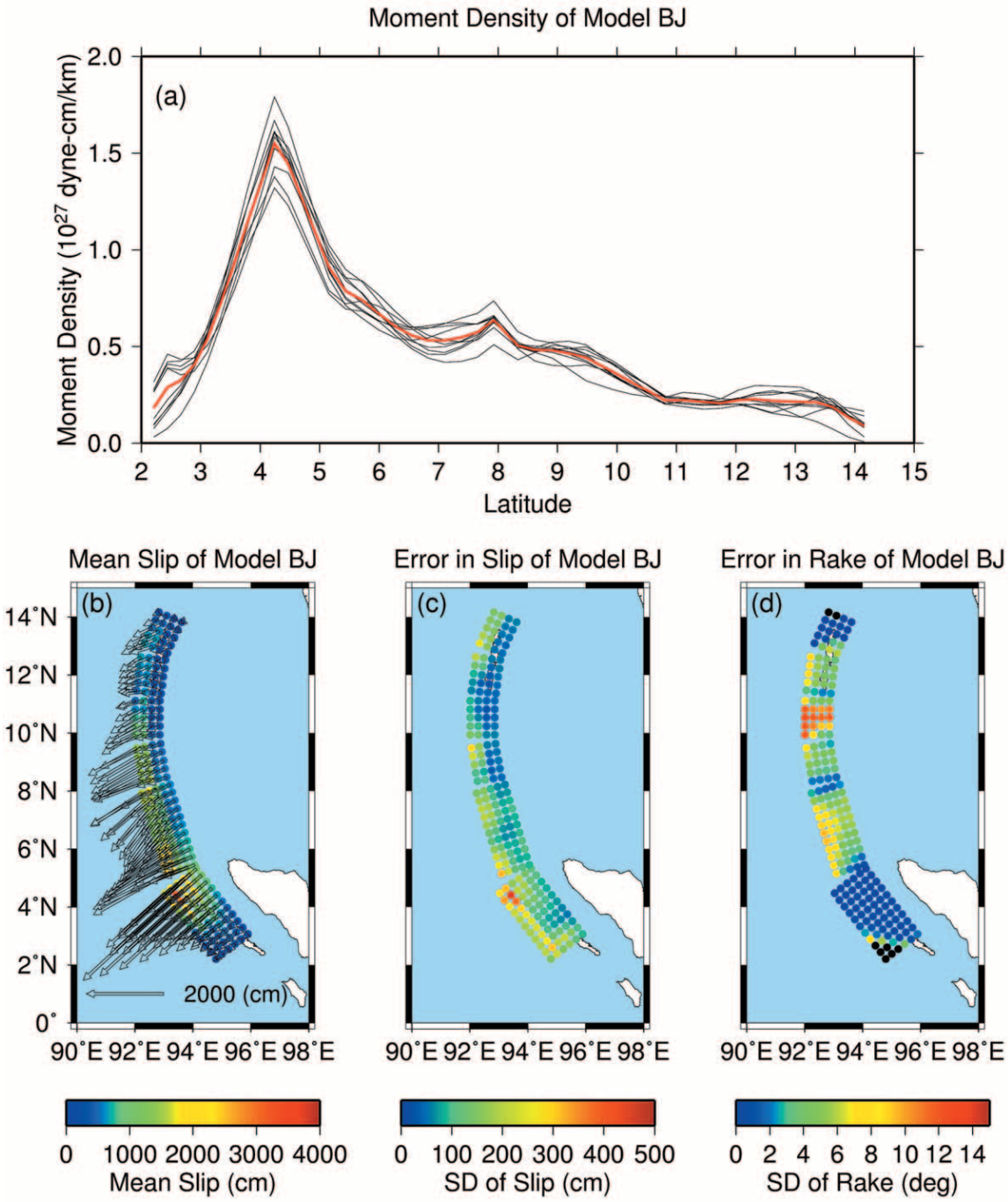

Figure 7. (a) Moment density obtained from a random station-selection analysis for fault-geometry model B. Black curves indicate the moment density inverted from each random 50% subset of seismic and GPS stations. The thick red curve represents the mean of 10 moment-density curves. (b) Mean slip distribution from the 10 cases. (c) Plot showing one standard deviation of slip in centimeters. Note that the color scale used to show the standard deviation in slip is about one-tenth of the scale used to plot the mean slip. (c) Plot showing the one standard deviation variation of the rake direction (degrees). For the same analysis for fault-geometry model A (Ⓔ see Figure S8 in the electronic edition of BSSA).

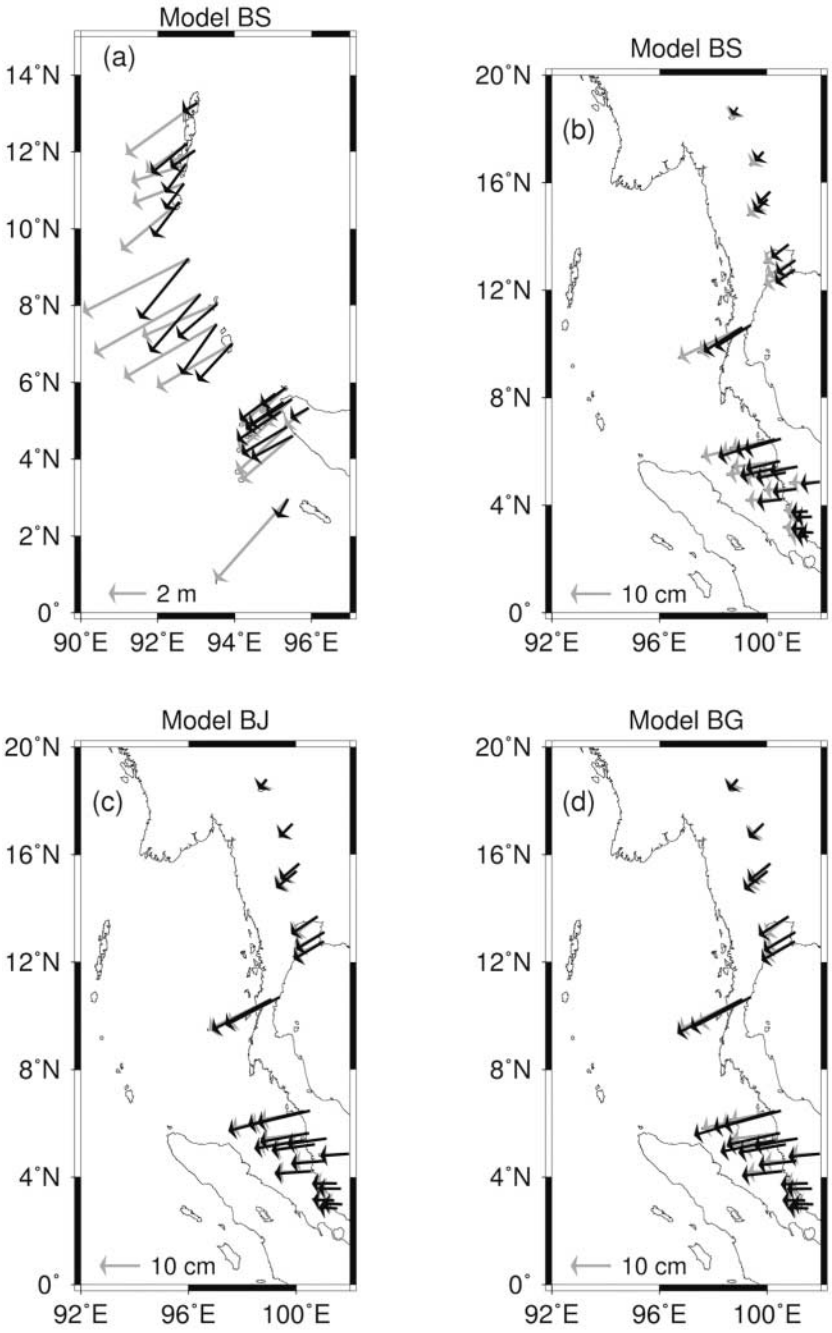

Figure 8. (a) Comparison between observed (gray) and synthetic (black) GPS vectors for the BS slip model (inversion of seismic data on uniform dip rupture). Modeled GPS vectors underestimate the observations. (b) Same as (a) for GPS sites on the Malaysian Peninsula located at larger distances from the rupture, which were not used in any of our inversions. (c) Same as (b) for the BJ slip model. Although offsets are slightly overestimated, the fit to far-field GPS offsets is very good. (d) Same as (b) for slip model BG. For geometry model A (Ⓔ see Figure S9 in the electronic edition of BSSA).

the high-slip region extends up to 10° N. This area of maximum slip was found to largely control the fit to the seismic-waveform data. The GPS data identify significantly more slip along the northern portion of the rupture than captured by seismic data alone, as was found in previous studies. In conclusion we find that the seismic and geodetic data complement each other well and allow us to determine a reliable kinematic description of the great 2004 Sumatra–Andaman earthquake.

Acknowledgments

We thank IRIS and GEOSCOPE for providing seismic data. GPS data used in this study were collected by the Survey of India (SOI), BAKOSURTANAL, the Tectonics Observatory at Caltech, and the Indonesian Institute of Sciences (LIPI). Figures were prepared using GMT (Wessel and Smith, 1991). We thank Susan Bilek and an anonymous reviewer for helpful comments. This is Berkeley Seismological Laboratory Contribution 06-11.

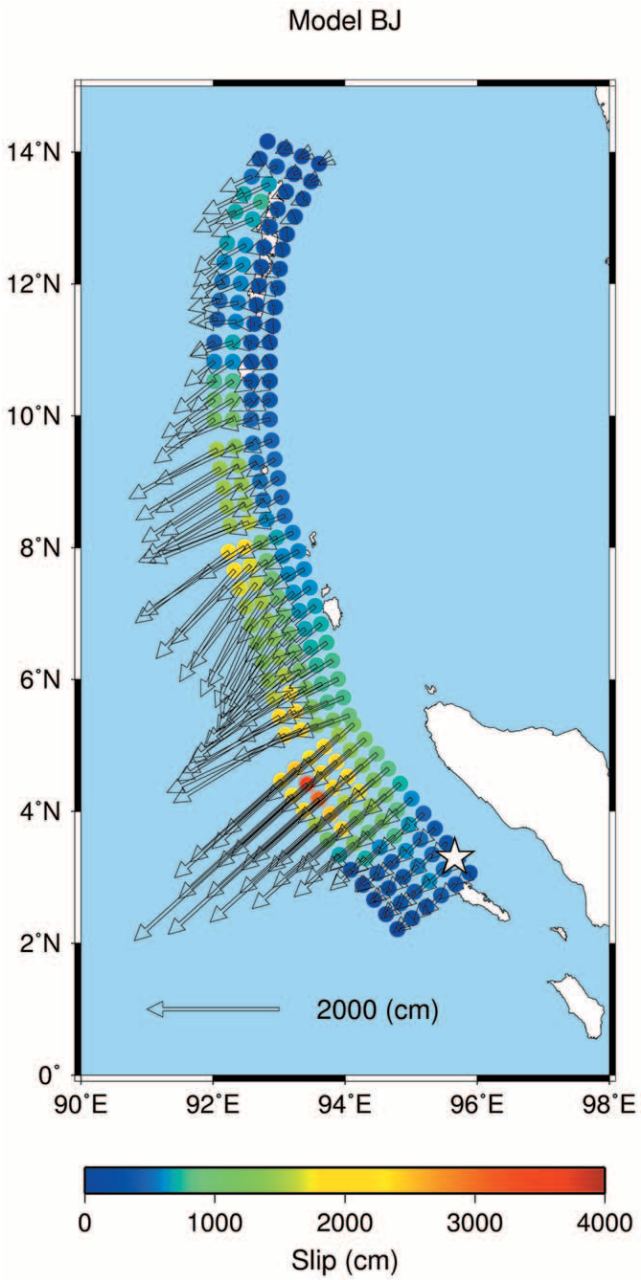

Figure 9. The preferred slip-distribution model from joint inversion of seismic waveforms and GPS static offsets over geometry model B.

References

Ammon, C. J., C. Ji, H.-K. Thio, D. Robinson, S. Ni, V. Hrorleifsdottir, H. Kanamori, T. Lay, S. Das, D. Helmberger, G. Ichinose, J. Polet, and D. Wald (2005). Rupture process of the 2004 Sumatra-Andaman earthquake, *Science* **308,** 1133–1139.

Banerjee, P., F. Pollitz, and R. Bürgmann (2005). The size and duration of the Sumatra-Andaman earthquake from far-field static offsets, *Science* **308,** 1769–1772.

Banerjee, P., F. Pollitz, B. Nagarajan, and R. Bürgmann (2007). Coseismic slip distributions of the 26 December 2004 Sumatra–Andaman and 28 March 2005 Nias earthquakes from GPS static offsets, *Bull. Seism. Soc. Am.* **97,** no. 1A, S86–S102.

Bilham, R., R. Engdahl, N. Feldi, and S. P. Satyabala (2005). Partial and complete rupture of the Indo-Andaman plate boundary 1847–2004, *Seism. Res. Lett.* **76,** 299–311.

de Groot-Hedlin, C. D. (2005). Estimation of the rupture length and velocity of the Great Sumatra earthquake of Dec 26, 2004 using hydroacoustic signals, *Geophys. Res. Lett.* **32,** L11303, doi 10.1029/2005GL022695.

Dreger, D., and A. Kaverina (2000). Seismic remote sensing for the earthquake source process and near-source strong shaking: A case study of the October 16, 1999 Hector Mine earthquake, *Geophys. Res. Lett.* **27,** 1941–1944.

Dziewonski, A. M., and D. L. Anderson (1981). Preliminary reference Earth model (PREM), *Phys. Earth Planet. Interiors* **25,** 297–356.

Engdahl, E. R., A. Villasenor, H. R. DeShon, and C. H. Thurber (2007). Teleseismic relocation and assessment of seismicity (1918–2005) in the region of the 2004 M_w 9.0 Sumatra-Andaman and 2005 M_w 8.6 Nias Island great earthquakes, *Bull. Seism. Soc. Am.* **97,** no. 1A, S43–S61.

Fine, I. V., A. B. Rabinovich, and R. E. Thomson (2005). The dual source region for the 2004 Sumatra tsunami, *Geophys. Res. Lett.* **32,** L16602, doi 10.1029/2005GL023521.

Global Centroid Moment Tensor (CMT) Project catalog search, www.globalcmt.org/CMTsearch.html (last accessed December 2005).

Hanks, T. C., and H. Kanamori (1979). A moment magnitude scale, *J. Geophys. Res.* **84,** 2348–2350.

Hartzell, S. H., and T. H. Heaton (1983). Inversion of strong ground motion and teleseismic waveform data for the fault rupture history of the 1979 Imperial Valley, California, earthquake, *Bull. Seism. Soc. Am.* **73,** 1553–1583.

Ishii, M., P. M Shearer, H. Houston, and J. E. Vidale (2005). Extent, duration and speed of the 2004 Sumatra Andaman earthquake imaged by the Hi-Net array, *Nature* **435,** 933–936.

Kaverina, A., D. Dreger, and E. Price (2002). The combined inversion of seismic and geodetic data for the source process of the 16 October 1999 Mw 7.1 Hector Mine, California, earthquake, *Bull. Seism. Soc. Am.* **92,** 1266–1280.

Krüger, F., and M. Ohrnberger (2005). Tracking the rupture of the Mw = 9.3 Sumatra earthquake over 1,150 km at teleseismic distance, *Nature* **435,** 937–939.

Lay, T., H. Kanamori, C. J. Ammon, M. Nettles, S. N. Ward, R. C. Aster, S. L. Beck, S. L. Bilek, M. R. Brudzinski, R. Butler, H. R. DeShon, G. Ekström, K. Satake, and S. Sipkin (2005). The Great Sumatra-Andaman Earthquake of 26 December 2004, *Science* **308,** 1127–1133.

Lomax, A. (2005). Rapid estimation of rupture extent for large earthquakes: application to the 2004, M9 Sumatra-Andaman mega-thrust, *Geophys. Res. Lett.* **32,** L10314, doi 10.1029/2005GL022437.

Ni, S., H. Kanamori, and D. Helmberger (2005). Energy radiation from the Sumatra earthquake, *Nature* **434,** 582.

Park, J. T., R. A. Song, J. Tromp, E. Okal, S. Stein, G. Roult, E. Clevede, G. Laske, H. Kanamori, P. Davis, J. Berger, C. Braienberg, M. V. Camp, X. Lei, H. Sun, H. Xu, and S. Rosat (2005). Earth's free Oscillations Excited by the 26 December 2004 Sumatra-Andaman Earthquake, *Science* **308,** 1139–1144.

Somerville, P., K. Irikura, R. Graves, S. Sawada, D. Wald, N. Abrahamson, Y. Iwasaki, T. Kagawa, N. Smith, and A. Kowada (1999). Characterizing crustal earthquake slip models for the prediction of strong ground motion, *Seism. Res. Lett.* **70,** 59–80.

Song, Y. T., C. Ji, L.-L. Fu, V. Zlotnicki, C. K. Shum, and Y. Yi (2005). The 26 December 2004 tsunami source estimated from satellite radar altimetry and seismic waves, *Geophys. Res. Lett.* **32,** L20601, doi 10.1029/2005GL023683.

Stein, S., and E. A. Okal (2005). Speed and size of the Sumatra earthquake, *Nature* **434,** 581–582.

Subarya, C., M. Chlieh, L. Prawirodirdjo, J.-P. Avouac, Y. Bock, K. Sieh, A. Meltzner, D. Natawidjaja, and R. McCaffrey (2006). Plate-

boundary deformation associated with the Great Sumatra-Andaman earthquake, *Nature* **440,** 46–51.

Tolstoy, M., and D. R. Bohnenstiehl (2005). Hydroacoustic constraints on the rupture duration, length, and speed of the great Sumatra-Andaman earthquake, *Seism. Res. Lett.* **76,** 419–425.

Tsai, V. C., M. Nettles, G. Ekstrom, and A. M. Dziewonski (2005). Multiple CMT source analysis of the 2004 Sumatra earthquake, *Geophys. Res. Lett.* **32,** L17304, doi 10.1029/2005GL023813.

Vigny, C., W. J. F. Simons, S. Abu, R. Bamphenyu, C. Satirapod, N. Choosakul, C. Subarya, A. Socquet, K. Omar, H. Z. Abidin, and B. A. C. Ambrosius (2005). Insight into the 2004 Sumatra-Andaman earthquake from GPS measurements in southeast Asia, *Nature* **436,** 201–206.

Wang, R., F. L. Lorenzo, and F. Roth (2003). Computation of deformation induced by earthquakes in multi-layered elastic crust — FORTRAN programs EDGRN/EDCMP, *Comput. Geosci.* **29,** 195–207.

Wessel, P., and W. H. F. Smith (1991). Free software helps map and display data, *EOS* **72,** 445–446.

Berkeley Seismological Laboratory
University of California
Berkeley, California 94720-4760

Manuscript received 16 January 2006.